PHYSICAL REVIEW B **66**, 014431 (2002)

Domain state model for exchange bias. II. Experiments

J. Keller, P. Miltényi, B. Beschoten,* and G. Güntherodt
2.Physikalisches Institut, RWTH Aachen, 52056 Aachen, Germany

U. Nowak† and K. D. Usadel
Theoretische Tieftemperaturphysik, Gerhard-Mercator-Universität Duisburg, 47048 Duisburg, Germany

(Received 15 August 2001; published 17 July 2002)

The exchange bias coupling at ferro-/antiferromagnetic interfaces of epitaxially grown Co/CoO bilayers can be intentionally enhanced and controlled by diluting the antiferromagnetic CoO layer, i.e., by introducing (i) nonmagnetic substitutions ($Co_{1-x}Mg_xO$) or (ii) Co deficiencies ($Co_{1-y}O$). All intentional nonmagnetic cations or defects were placed away from the interface throughout the whole volume part of the antiferromagnetic layer. This way the roughness at the Co/CoO interface was kept practically the same. For both types of defects, the exchange bias field can be increased by a factor of 3 to 4. Hence, exchange bias is primarily not due to roughness at the interface but rather can be controlled by the defects in the volume part of the antiferromagnetic layer. We systematically investigate the dilution dependence of various phenomena of exchange bias, such as the vertical magnetization shift of the hysteresis loop, temperature dependence, training effect, cooling field dependence, and antiferromagnetic layer thickness dependence. All these phenomena are directly compared to results from Monte Carlo simulations and are shown to be consistently described by the domain state model for exchange bias. The combined experimental and theoretical findings suggest that the origin of exchange bias in Co/CoO results from a domain state in the volume part of the antiferromagnet stabilized by the defects.

DOI: 10.1103/PhysRevB.66.014431 PACS number(s): 75.70.Cn, 75.70.Kw, 75.30.Gw, 75.50.Lk

I. INTRODUCTION

Direct exchange coupling at the interface between a ferromagnetic (FM) and an antiferromagnetic (AFM) layer may result in exchange biasing, which induces an unidirectional anisotropy of the FM layer. The unidirectional anisotropy causes a shift of the hysteresis loop along the magnetic field axis. The magnitude of the field shift is called the exchange bias (EB) field B_{EB}. Usually, the EB shift occurs after cooling the system with a saturated FM layer below the Néel temperature of the AFM layer or by layer deposition in an external magnetic field. Despite four decades of research since its discovery[1,2] and the commercially available magnetic sensor devices,[3,4] the microscopic understanding of the EB effect is still not fully established.[5]

In a recent paper,[6] we reported on EB studies in Co/CoO bilayers as a function of volume defects in the antiferromagnet. Of particular importance in this study was the observation that nonmagnetic defects in the volume of the AFM layer can enhance the exchange bias by a factor of up to 3. The nonmagnetic defects (dilution) in CoO were realized in two ways: (i) by overoxidizing CoO leading to Co deficiencies in $Co_{1-y}O$ or (ii) by substituting nonmagnetic Mg ions for magnetic Co in $Co_{1-x}Mg_xO$. For all samples investigated a 0.4-nm-thick CoO layer with minimum defect concentration was placed at the interface. Therefore, in these systems the observed EB is primarily not due to disorder or defects at the interface. Rather, the strong dependence of the EB field on the dilution of the AFM layer was concluded to have its origin in the formation of a domain state in the volume of the AFM layer. This domain state gives rise to a small but significant excess of magnetic moments at the FM/AFM interface, which is irreversible under FM magnetization reversal. These uncompensated moments cause and control exchange bias.

The ‘‘domain state’’ (DS) model gives a description of exchange bias, which is supported by Monte Carlo (MC) simulations.[6,7] The model links the physics of diluted antiferromagnets in an external field (Refs. 8 and 9) to the coupling mechanisms of exchange-coupled magnetic layers.

Malozemoff has already pointed out the relevance of AFM domains for the exchange bias effect due to interface roughness.[10–12] In the DS model, however, the stabilization of AFM domains is not due to interfacial roughness, but rather induced and stabilized by the existence of volume defects in the AFM layer. Indeed, it appears reasonable to assume that any deviation from a perfect AFM crystalline structure (disorder in the AFM layer), such as defects, or grain or twin boundaries, can favor the formation of magnetic domains and by that affect the EB coupling. Here, nonmagnetic volume defects (dilution) in the antiferromagnet were chosen since the degree of dilution can easily and reproducibly be adjusted during sample deposition by the AFM stoichiometry.

The magnetic linear dichroism effect in soft-x-ray absorption has recently been used to probe as well as to image the domains and the structure in AFM films.[13–16] This spectroscopy technique has also been employed to image both FM and AFM domains in FM/AFM exchange-coupled systems.[17–20] These domains have been shown to be coinciding and give evidence of EB coupling on a local scale.

In the present paper we systematically investigate a variety of the most characteristic EB phenomena for both $Co/Co_{1-x}Mg_xO$ and $Co/Co_{1-y}O$ bilayer systems as a function of dilution. These phenomena include, besides EB field and coercivity field, the shape and vertical shift of the hys-

0163-1829/2002/66(1)/014431(11)/$20.00

teresis loops, the temperature dependence of the EB field, the training effect, the cooling field dependence, and the dependence of the EB on the AFM layer thickness. Each of these phenomena as a function of dilution is directly compared with results from MC simulations and discussed within the DS model, which is shown to provide a consistent description of the origin of EB as well as of a variety of related phenomena.

The paper is organized as follows. The following section describes the sample preparation by molecular-beam epitaxy (MBE). In Sec. III the dilution dependence of the structural properties is investigated by reflection high-energy electron diffraction (RHEED), high-angle x-ray diffraction, and atomic force microscopy. Typical EB phenomena are presented in Sec. IV. For easier comparison, these effects are discussed in exactly the same order as in the preceding theoretical part of the paper.[7] Finally, we conclude in the last section.

II. SAMPLE PREPARATION

The samples were prepared on (0001)-oriented sapphire substrates in a MBE chamber. Prior to film deposition the substrates were heated to $T=775$ K for 1 h in order to outgas the substrate holder and then cooled to the Co growth temperature of $T_{\mathrm{Co}}=575$ K. The layered sample structure is schematically illustrated in the inset of Fig. 3(a) below. First, a 6-nm-thick Co layer was deposited by electron-beam evaporation at a rate of 0.2 nm/min, which was subsequently annealed at a temperature of $T=775$ K for 10 min. Thereafter, a 0.4-nm-thick CoO layer was deposited for all samples at a substrate temperature of $T_{\mathrm{oxide}}=350$ K and an oxygen pressure of $p(\mathrm{O}_2)=3.3\times10^{-7}$ mbar with a rate of 0.3 nm/min. Note that the RHEED pattern (see Sec. III) of the Co layer completely disappears after initially exposing the Co layer to an oxygen pressure of $p(\mathrm{O}_2)=3.3\times10^{-7}$ mbar prior to CoO deposition. This demonstrates that the Co/CoO interface is created over the entire Co layer even before depositing the 0.4 nm CoO interface layer, which then ensures a continuous and homogeneous CoO layer at the FM/AFM interface. This procedure leads to practically identical FM/AFM interfaces for all samples investigated at the lowest possible interface defect concentration, independent of the dilution of the following 20-nm-thick AFM layer.

On top of this CoO interface layer two different sets of diluted antiferromagnetic layers were deposited. In a first set of samples CoO was diluted with nonmagnetic MgO forming $\mathrm{Co}_{1-x}\mathrm{Mg}_x\mathrm{O}$. Co and MgO were coevaporated in an oxygen atmosphere of $p(\mathrm{O}_2)=3.3\times10^{-7}$ mbar at a substrate temperature of $T_{\mathrm{oxide}}=350$ K and a deposition rate of 0.3 nm/min. The Mg concentration was varied between $x=0$ and $x=1$, while the AFM layer thickness was kept constant at 20 nm. For a second set of samples, nonmagnetic defects were realized by overoxidation of CoO yielding Co-deficient $\mathrm{Co}_{1-y}\mathrm{O}$. The Co deficiency y was controlled by varying the oxygen pressure during evaporation between $p(O_2)=3.3\times10^{-7}$ mbar and 1.0×10^{-5} mbar, while growth temperature, growth rate, and AFM layer thickness were all identical to the first set of samples.

Two additional sets of samples were prepared to study the dependence of EB on the AFM layer thickness. For these samples the AFM interface layer was similarly prepared as described above, although this time we did not deposit the initial 0.4-nm-thick CoO layer. The AFM layer thickness was varied between 1 nm and 50 nm. The two sets of samples were prepared with low $[p(\mathrm{O}_2)=3.3\times10^{-7}$ mbar$]$ and with intermediate $[p(\mathrm{O}_2)=5\times10^{-6}$ mbar$]$ oxygen pressure during evaporation. All thicknesses and the roughness of the different layers were controlled by a calibrated quartz microbalance and *ex situ* atomic force microscopy, respectively.

III. STRUCTURAL PROPERTIES

All samples were characterized *in situ* by RHEED and low energy electron diffraction (LEED). The RHEED patterns of the substrate and of the different layers of which the samples consist are depicted in Figs. 1(a)–1(d). The left panels show the diffraction patterns for the electron beam incident parallel to the $[\overline{11}20]$ direction $(0°)$ of the (0001)-oriented sapphire substrate and the right panels for the beam parallel to the $[\overline{1}010]$ direction $(30°)$. The spot separation in the RHEED image of the sapphire substrate in the 30° direction [Fig. 1(a), right panel] is about $\sqrt{3}$ times the spot separation in the $0°$ direction [Fig. 1(a), left panel]. This is consistent with the hexagonal surface symmetry of the sapphire (0001) substrate.[21] For a 6-nm-thick Co layer on the sapphire substrate in Fig. 1(b) the same ratio is found but the two directions are interchanged. From this we conclude that Co grows epitaxially in either fcc (111) or in hcp (0001) orientation, which only differ in their so-called ABAB or ABCABC stacking order along the surface normal.[21] Additional LEED investigations (not shown) reveal clearly the corresponding sixfold symmetry.

RHEED images of the 20-nm-thick $\mathrm{Co}_{1-y}\mathrm{O}$ layers are shown in Fig. 1(c) and 1(d) grown at oxygen pressures of $p(\mathrm{O}_2)=3.3\times10^{-7}$ mbar and 1.0×10^{-5} mbar, respectively. All diffraction patterns from the AFM layers show a transmission image, i.e., diffraction from a rough surface with islands.[22] In order to explain the observed RHEED patterns a (111) orientation of fcc $\mathrm{Co}_{1-y}\mathrm{O}$ is assumed. The calculated diffraction patterns are shown in Fig. 1(e). The filled circles represent the reciprocal lattice points of the undiluted CoO fcc lattice.

In the $0°$ direction, the calculated pattern of filled circles [Fig. 1(e)] fits to the RHEED image of the $\mathrm{Co}_{1-y}\mathrm{O}$ layer prepared at low oxygen pressure [Fig. 1(c), left panel]. For the samples prepared at higher oxygen pressures, additional diffraction spots [open circles in Figs. 1(e) and 1(f)] appear at half the distance between the filled circles showing an additional structure with approximately twice the lattice constant in real space. We believe that these additional spots are due to the formation of $\mathrm{Co}_3\mathrm{O}_4$ upon dilution, which is also consistent with results from x-ray diffraction (see below). We conclude that almost defect-free CoO is deposited at low oxygen pressure $[p(\mathrm{O}_2)=3.3\times10^{-7}$ mbar$]$, while for higher oxygen pressures Co-deficient $\mathrm{Co}_{1-y}\mathrm{O}$ is formed. To further investigate the formation of the additional phase with

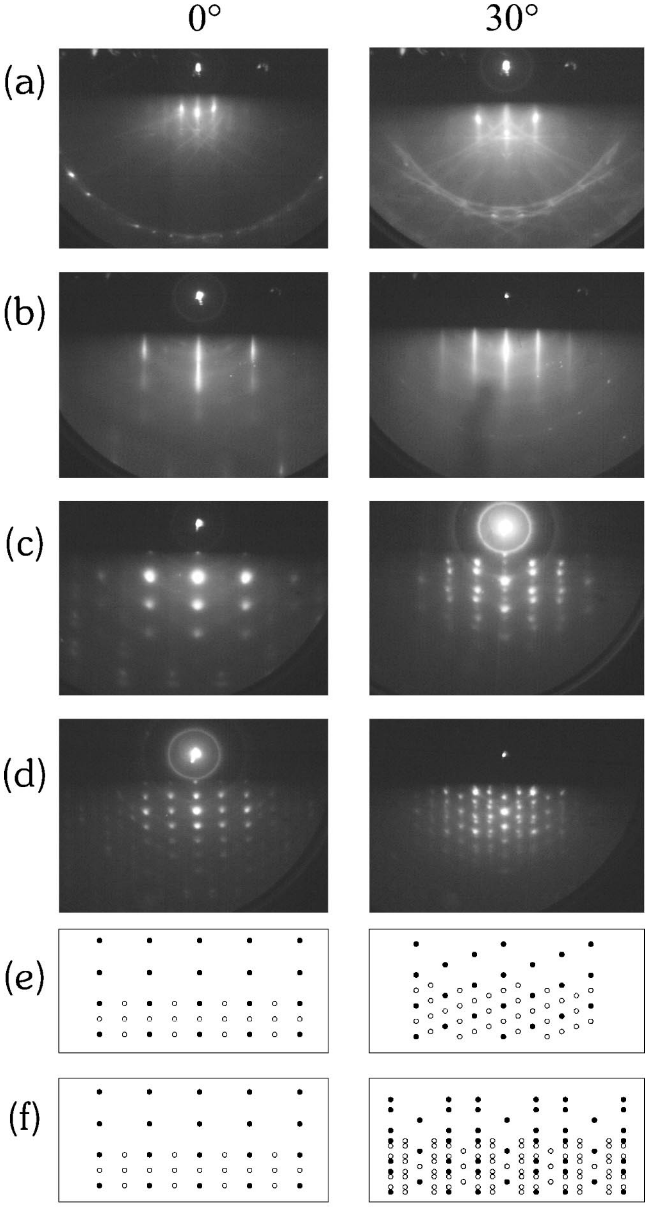

FIG. 1. RHEED images of the (a) (0001)-oriented sapphire substrate, (b) 6-nm Co layer on sapphire, and two 20-nm $Co_{1-y}O$ layers prepared at (c) $p(O_2)=3.3\times10^{-7}$ mbar and at (d) $p(O_2)=1.0\times10^{-5}$ mbar on a 6-nm-thick Co layer. (e) and (f): Simulated reflections of the diffraction patterns of $Co_{1-y}O$ (111); (e) without twins and (f) with 60° in-plane twins. Only solid dots fulfill the diffraction condition for the CoO fcc lattice. The two vertical panels show the patterns for 0° and 30° in-plane orientation of the incident electron beam relative to the sapphire $[\overline{11}20]$ axis.

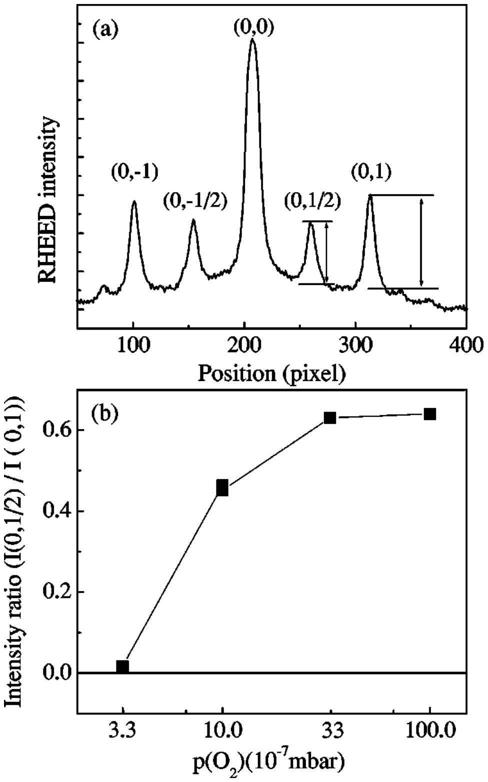

FIG. 2. (a) Line scan of the RHEED image shown in Fig. 1(d), left panel, for a $Co_{1-y}O$ layer prepared at $p(O_2)=1.0\times10^{-5}$ mbar. (b) Dilution dependence of intensity ratio between the additional (0,1/2) spot for overoxidized $Co_{1-y}O$ and the (0,1) reflections for the CoO fcc structure.

increasing oxygen pressure, we analyze the evolution of the RHEED intensity of the (0,1/2) spot [open circles in Figs. 1(e) and 1(f)] as a function of oxygen pressure. Figure 2(a) shows a line scan through the RHEED diffraction pattern of $Co_{1-y}O$ prepared at high oxygen pressure [$p(O_2)=1\times10^{-5}$ mbar]. The (0,1) peak corresponds to the undiluted fcc lattice of CoO, while the (0,1/2) peak appears for Co-deficient $Co_{1-y}O$. The relative intensity of the (0,1/2) and (0,1) peaks is strongly increasing as a function of oxygen pressure as seen in Fig. 2(b). This supports the notion that the number of volume defects in the AFM layer can be controlled by the oxygen pressure during deposition, i.e., the number of defects is continuously increasing with increasing oxygen pressure.

We now discuss the RHEED patterns along the 30° direction in Fig. 1 (right panels). The calculated RHEED pattern in Fig. 1(e) does not reproduce the double spot structures as observed for all oxygen concentrations [see Figs. 1(c) and 1(d), right panels]. In order to explain these diffraction patterns, we furthermore have to assume that $Co_{1-y}O$ grows in a twinned structure where crystallites are oriented 60° relative to each other [compare Fig. 1(f) with Figs. 1(c) and 1(d), right panels]. Similar to the 0° direction the undiluted sample [Fig. 1(c)] only shows reflections from a CoO fcc lattice, while the diluted samples also show reflections from the defect phase.

The main experimental features of the RHEED investigation of the $Co_{1-y}O$ layers are (i) the number of defects in $Co_{1-y}O$ continuously increases with increasing oxygen pressure during evaporation and (ii) the layers grow with 60° twins. The same qualitative findings were observed in Mg-diluted CoO layers (not shown). In the following we will refer to the samples with the lowest defect concentration [$p(O_2)=3.3\times10^{-7}$ mbar and $x(\mathrm{Mg})=0.0$] as unintentionally diluted.

Additional structural characterization was carried out by

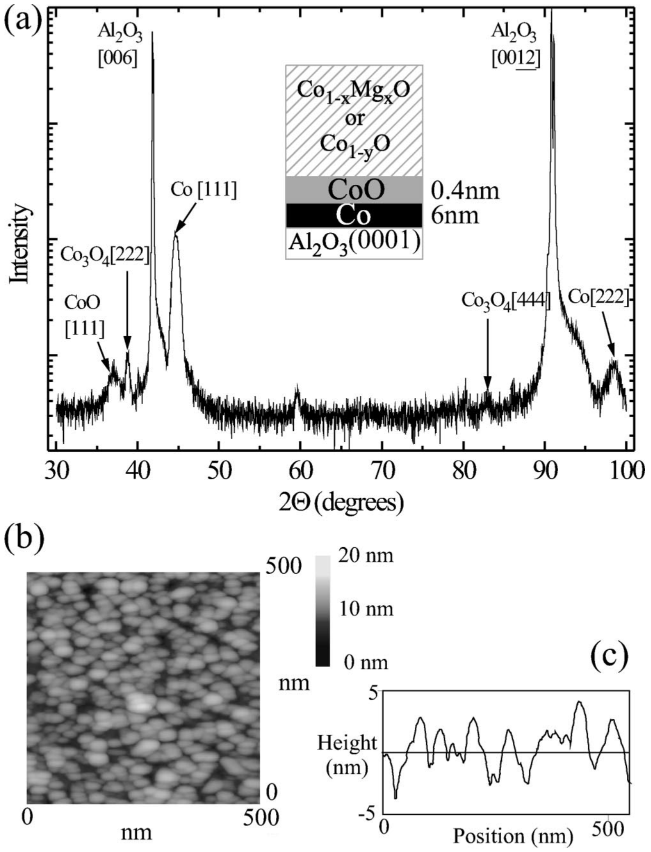

FIG. 3. (a) High-angle x-ray diffraction ($\lambda = 0.154\,18$ nm) for Co/Co$_{1-y}$O with Co$_{1-y}$O prepared at $p(O_2) = 3\times10^{-6}$ mbar. The sample structure is schematically depicted in the inset. (b) Atomic force microscopy image of a 20-nm-thick Co$_{1-y}$O layer prepared at $p(O_2) = 3\times10^{-6}$ mbar layer on a 6-nm-thick Co layer. Crystallite sizes range between 25 and 35 nm. (c) Line scan of image.

ex situ x-ray diffraction using Cu K_α radiation ($\lambda = 0.154\,18$ nm). A high-angle θ-2θ scan of a Co/Co$_{1-y}$O bilayer with the antiferromagnet prepared at $p(O_2) = 3\times10^{-6}$ mbar is shown in Fig. 3(a). Besides prominent $[0\ 0\ l]$- Al$_2$O$_3$ substrate peaks, only [1 1 1] reflections and those of higher order are seen for both Co and CoO, which is consistent with the RHEED results. In addition, [1 1 1]-oriented Co$_3$O$_4$ is observed.

To further investigate the surface of the Co$_{1-y}$O layers, *ex situ* atomic force microscopy images were taken. Figure 3(b) shows an atomic force microscope image for a 20-nm-thick Co$_{1-y}$O layer prepared at $p(O_2) = 3\times10^{-6}$ mbar on top of a 6-nm Co layer. As expected from the RHEED investigations a rough surface is found. The crystallite size ranges between 25 nm and 35 nm. As is seen from the line scan in Fig. 3(c), the surface has a peak-to-peak height variation of approximately 6 nm.

IV. MAGNETIC PROPERTIES

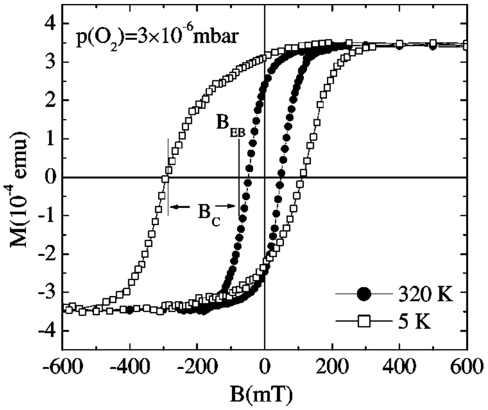

FIG. 4. Hysteresis loops of Co$_{1-y}$O/Co/Al$_2$O$_3$ (0001) at $T = 5$ K and $T = 320$ K with the Co$_{1-y}$O prepared at $p(O_2) = 3\times10^{-6}$ mbar. The exchange bias field B_{EB} and the coercivity field B$_C$ are indicated in the figure.

The magnetic characterization of the samples was performed using a superconducting quantum interference device (SQUID) magnetometer. The samples were cooled from 320 K, i.e., from above the Néel temperature T_N(CoO) $= 291$ K to 5 K in the presence of an external magnetic field $+B_{FC}$, oriented parallel to the plane of the film. Except for the explicit studies of the cooling field dependence (see Sec. IV E), a cooling field of $B_{FC} = 5$ T was chosen for all measurements presented. This value is larger than the saturation field of the ferromagnetic Co layer.

A. Hysteresis

Figure 4 shows typical hysteresis loops above ($T = 320$ K) and below ($T = 5$ K) the Néel temperature of a sample with the Co$_{1-y}$O layer grown at $p(O_2) = 3\times10^{-6}$ mbar. The loop at low temperature exhibits a large exchange bias shift B_{EB} towards negative magnetic fields, which is opposite to the cooling field direction. In addition, a strong increase in the coercivity field B_C is observed at 5 K compared to 320 K leading to a significant broadening of the width of the loops.

Like most conventional magnetization probes, SQUID magnetometry is not layer or element specific but rather measures the whole FM/AFM bilayer magnetization. In addition to the magnetization of the FM layer, both interface and volume magnetization of the diluted AFM layer will therefore contribute to the total magnetization. If the magnetization of the antiferromagnet is irreversible under field reversal, it can be identified as a vertical shift of the measured hysteresis loop. Such an AFM magnetization was first observed in hysteresis loops of Fe/FeF$_2$ and Fe/MnF$_2$.[23] Both, positive and negative vertical shifts were found and attributed to positive (ferromagnetic) and negative (antiferromagnetic) FM/AFM interface coupling, respectively. However, the origin of the induced moment could not directly be assigned to either interface or volume magnetization.

To investigate the change of the AFM magnetization with the number of introduced volume defects in the AFM layer, we performed high accuracy magnetization measurements of the vertical magnetization shift for both unintentionally diluted and oxygen-diluted samples grown at $p(O_2) = 3.3\times10^{-7}$ mbar and $p(O_2) = 3\times10^{-6}$ mbar, respectively. The shift was determined at $T = 20$ K and is given by

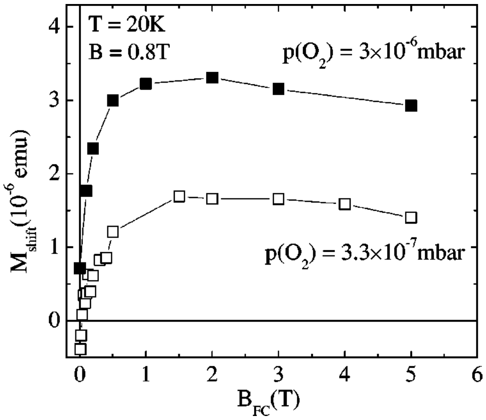

FIG. 5. Vertical magnetization shift M_{shift} vs cooling field B_{FC} for Co/Co$_{1-y}$O samples with Co$_{1-y}$O prepared at different oxygen pressures. Data are taken at $B=\pm 0.8$ T and $T=20$ K and are extracted as described in the text.

$M_{\text{shift}}=|M(B_+)|-|M(B_-)|$, where B_+ and B_- are chosen so that the FM layer is fully saturated with $|B_+|=|B_-|$. The data shown in Fig. 5 were taken at $B_\pm=\pm 0.8$ T. As is seen in Fig. 5, at large cooling fields M_{shift} is positive and overall increasing with dilution of the AFM layer at all cooling fields. This increase can directly be linked to the creation of additional volume defects in the AFM layer as shown by the above RHEED analysis. It further supports that a domain state is developed in the antiferromagnet after field cooling carrying a surplus magnetization, which increases with dilution. It is important to note that in our experiments we measure the total AFM surplus magnetization as was also investigated by similar magnetization probes in CoO/MgO multilayers[24] and Co$_x$Mg$_{1-x}$O powder samples.[25] Although, this surplus magnetization does not equal the irreversible domain state (IDS) magnetization m_{IDS} of the AFM interface layer defined in Sec. IV A of Ref. 7, we find striking qualitative agreement that the EB field indeed is proportional to the measured AFM magnetization (see the next section and Sec. IV E).

In the MC simulations,[7] contributions from both interface and bulk magnetization of the AFM layer can be separated. After zero-field cooling, the bulk of the AFM layer does not carry surplus magnetization (see Fig. 5 in Ref. 7), while it should dominate the total surplus magnetization for larger cooling fields. Indeed, we observe a strong reduction of M_{shift} for cooling fields below 1 T as is seen in Fig. 5. Thus, it is suggestive that the low-field AFM magnetization primarily originates from the AFM spins close to the interface. While for diluted samples, M_{shift} remains finite and positive for zero cooling field, it changes sign for unintentionally diluted samples. The former case is consistent with positive (ferromagnetic) FM/AFM interface coupling in Co/CoO (compare with AFM magnetization loops in MC simulations as shown in Fig. 4 of Ref. 7). This conclusion is also consistent with the cooling field dependence of the EB shift which will be discussed in Sec. IV E.

However, it has to be reemphasized that by SQUID magnetometry we do not only measure the IDS magnetization m_{IDS} of the AFM interface layer, which is responsible for the EB coupling in the DS model. Therefore, at present it is not clear as to how much the sign reversal of M_{shift} at $B_{\text{FC}}=0$ is related to the EB coupling.

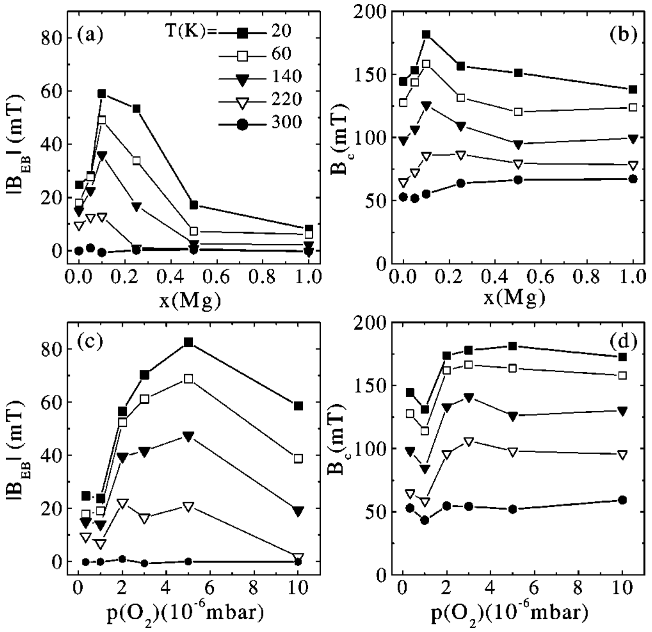

FIG. 6. (a) EB field and (b) coercivity field vs Mg concentration x in the Co$_{1-x}$Mg$_x$O layer for various temperatures. (c) EB field and (d) coercivity field vs oxygen pressure during deposition of the Co$_{1-y}$O layer at the same temperatures. Note that only absolute EB values are plotted. All lines are guides to the eye.

B. Influence of dilution

The dilution dependence of both the EB field $|B_{\text{EB}}|$ and coercivity field B_C for Mg-diluted Co$_{1-x}$Mg$_x$O samples is shown in the upper panels of Fig. 6, while in the lower panels of Fig. 6 analogous results of Co-deficient Co/Co$_{1-y}$O samples are depicted. The EB is enhanced by a factor of 3 to 4 for both types of defects in the AFM layer. Maximum enhancement is obtained for $x(\text{Mg})=0.1$ and $p(\text{O}_2)=5\times 10^{-6}$ mbar. Note that compared to our previous work,[6] we prepared additional Co-deficient samples at an oxygen pressure of $p(\text{O}_2)=5\times 10^{-6}$ mbar, which show the largest EB field of all samples. Within the DS model, the observed increase of the EB shift with an increasing number of defects can be related to the formation of volume domain walls, which preferentially pass through the nonmagnetic defects at no cost of exchange energy. This leads to the experimentally observed excess magnetization of the antiferromagnet. The increase of excess magnetization between unintentionally diluted samples $[x(\text{Mg})=0, p(\text{O}_2)=3.3\times 10^{-7}$ mbar$]$ and optimally diluted samples $[x(\text{Mg})=0.1$ or $p(\text{O}_2)=5\times 10^{-6}$ mbar$]$ is directly verified by the vertical magnetization shift of the hysteresis loop (see Sec. IV A). This strongly supports the fact that the domain state in the AFM layer as well as the EB effect is caused and controlled by the defects. For large dilution $[x(\text{Mg})>0.25; p(\text{O}_2)>5\times 10^{-6}$ mbar$]$ the EB again decreases as the antiferromagnetic order is increasingly suppressed and eventually the connectivity in the AFM lattice is lost. Residual EB at high dilutions [$x(\mathrm{Mg})=1.0$] has to be attributed to the 0.4-nm CoO interface layer and the underlying oxidized layer (see also Sec. IV C). A similar behavior is observed in other EB systems consisting of diluted metallic antiferromagnets.[26–28] It has also be shown that the EB can be enhanced by ion irradiation of the whole FM/AFM sample.[29]

MC simulations (see Fig. 6 of Ref. 7) qualitatively reproduce both the initial increase of EB with increasing dilution and its decrease at larger dilutions. However, the concentrations for optimally diluted samples significantly differ between experiment [$x(\mathrm{Mg})\approx 0.15$] and theory ($p\approx 0.6$). A possible origin of this difference is the presence of grain boundaries in the twinned AFM layer which reduce the domain-wall energy, thus leading to a finite EB without intentional dilution of the AFM layer as observed for the unintentionally diluted samples. This conclusion is consistent with the rather small EB found in untwinned and single crystalline antiferromagnets.[30–32] As seen in Figs. 6(a) and 6(c) the defect concentration for maximum EB depends on the temperature, i.e., it shifts towards smaller values at elevated temperatures, which is also qualitatively observed in MC simulations (see Fig. 6 in Ref. 7).

We next discuss the dilution dependence of the coercivity field B_C, which is shown in Figs. 6(b) and 6(d). Similar to the EB field, it changes nonmonotonically with dilution and shows maximum values at the same defect concentrations as the EB, although its relative changes are smaller than those observed in the EB field. Like the EB, the coercivity also strongly decreases with increasing temperature, which is common for many EB systems.[5] The change in coercivity with temperature is caused by the change in the coupling of the FM (Co) layer with the AFM (CoO) layer.

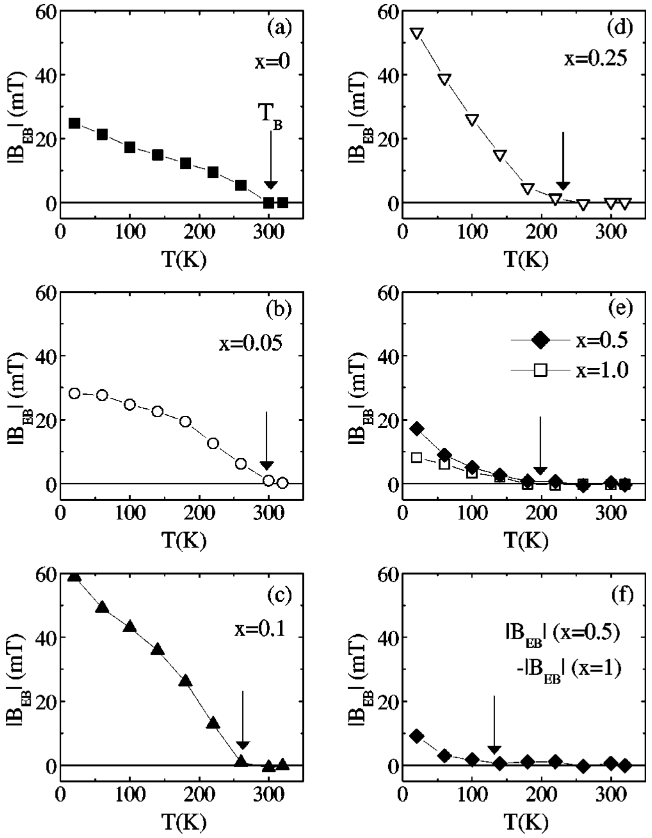

FIG. 7. (a)–(e) Temperature dependence of EB field for the Mg-diluted Co/$\mathrm{Co}_{1-x}\mathrm{Mg}_x\mathrm{O}$ samples with $x=0$, 0.05, 0.1, 0.25, 0.5, and 1.0 as shown in Fig. 6(a). (f) Difference in EB fields for samples with $x=0.5$ and $x=1.0$. The blocking temperature is marked by an arrow in each figure.

C. Temperature dependence

The temperature dependence of the exchange bias field $|B_{\mathrm{EB}}|$ for the Mg-diluted Co/$\mathrm{Co}_{1-x}\mathrm{Mg}_x\mathrm{O}$ samples is shown in Figs. 7(a)–7(e) at the same Mg concentrations as in Fig. 6(a). For all samples the EB field is monotonically increasing with decreasing temperature. It almost varies linearly with temperature near optimum dilution [$x(\mathrm{Mg})=0.1$ and $x(\mathrm{Mg})=0.25$], while it saturates at low temperatures and low dilutions [Figs. 7(a) and 7(b)]. The former dependence agrees well with the temperature behavior as obtained by MC simulations near optimum dilution (see Fig. 8 in Ref. 7).

The results are described by the DS model as follows: A metastable domain state is frozen at low temperatures after field cooling, which inhibits domain-wall motion. Thermally activated domain-wall motion becomes more favorable at elevated temperatures, which leads to a reduction of m_{IDS} and thus to a decrease of the exchange bias field as observed experimentally.

The EB vanishes above the so-called blocking temperature T_B, which might significantly differ from the Néel temperature T_N of the antiferromagnet.[7,33] Its monotonic decrease with increasing Mg dilution in Co/$\mathrm{Co}_{1-x}\mathrm{Mg}_x\mathrm{O}$ samples can be seen by the arrows in Figs. 7(a)–7(e) and is also plotted in Fig. 8. We observe a similar but weaker decrease of T_B for the Co/$\mathrm{Co}_{1-y}\mathrm{O}$ samples (not shown). Note that the blocking temperature is not completely diminished for the fully diluted sample with $x(\mathrm{Mg})=1.0$. As already discussed above, we attribute this remaining EB coupling to

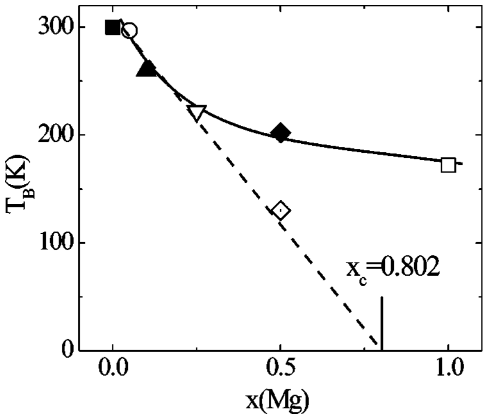

FIG. 8. Dilution dependence of blocking temperature T_B for the Mg diluted Co/$\mathrm{Co}_{1-x}\mathrm{Mg}_x\mathrm{O}$ samples as shown in Fig. 7. For $x=0.5$ the lower T_B (dot-center diamond) is taken from Fig. 7(f). All lines are guides to the eye. The percolation threshold x_c for a three-dimensional fcc lattice with nearest neighbor interaction is included.

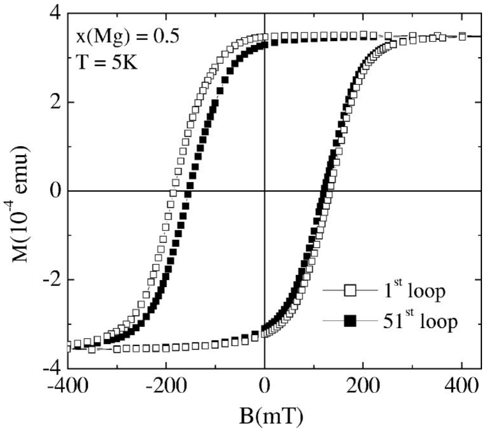

FIG. 9. Training effect of Co/Co$_{1-x}$Mg$_x$O sample with $x=0.5$. Plotted are the first and the 51st hysteresis loops at $T=5$ K after field cooling.

the CoO interface layer and the underlying oxidized layer. This residual EB coupling is likely also to be relevant for the temperature dependence of the EB field for the sample with $x(\mathrm{Mg})=0.5$, as can be seen in Fig. 7(e). To further separate the contributions to the EB coupling from the undiluted interface layer from that of the diluted AFM volume layer, we subtract the EB fields for the sample with $x(\mathrm{Mg})=1.0$ from the sample with $x(\mathrm{Mg})=0.5$, which is depicted in Fig. 7(f). The resulting blocking temperature, which is strongly reduced, is also included in Fig. 8 at $x(\mathrm{Mg})=0.5$. Note that all other samples do not show any significant change in blocking temperature when performing a similar subtraction (not shown).

As is seen in Fig. 8, the modified blocking temperatures linearly decrease with increasing Mg dilution of the AFM volume layer (dashed line). In particular, the extrapolated dilution, above which EB coupling vanishes completely ($T_B \rightarrow 0$), is close to the percolation threshold ($x_c=0.802$) for antiferromagnetism in a three-dimensional fcc lattice with nearest-neighbor interaction.[34] This supports the notion that no global EB coupling remains once the connectivity of the AFM spin lattice is lost.

D. Training effect

Most thin-film EB systems show a reduction of the EB shift upon subsequent magnetization reversals of the FM layer,[5,35,36] which is the so-called training effect. For all Mg-diluted Co/Co$_{1-x}$Mg$_x$O samples we measured the training effect at $T=5$ K after field cooling in $B_{\mathrm{FC}}=5$ T. Typical magnetization reversals corresponding to the first and 51st hysteresis loops are shown in Fig. 9 for the sample with $x(\mathrm{Mg})=0.5$. Besides a clear, but rather small reduction of the exchange bias shift, a decrease of the coercivity field is observed. The training effect implies that during magnetization reversal the FM layer does not reverse homogeneously nor reversibly. According to the DS model, the training effect is due to a rearrangement of the AFM domain structure, which results in a partial loss of the IDS magnetization m_{IDS} of the AFM interface layer during field cycling.[7] This magnetization loss leads to a reduction of the EB shift.

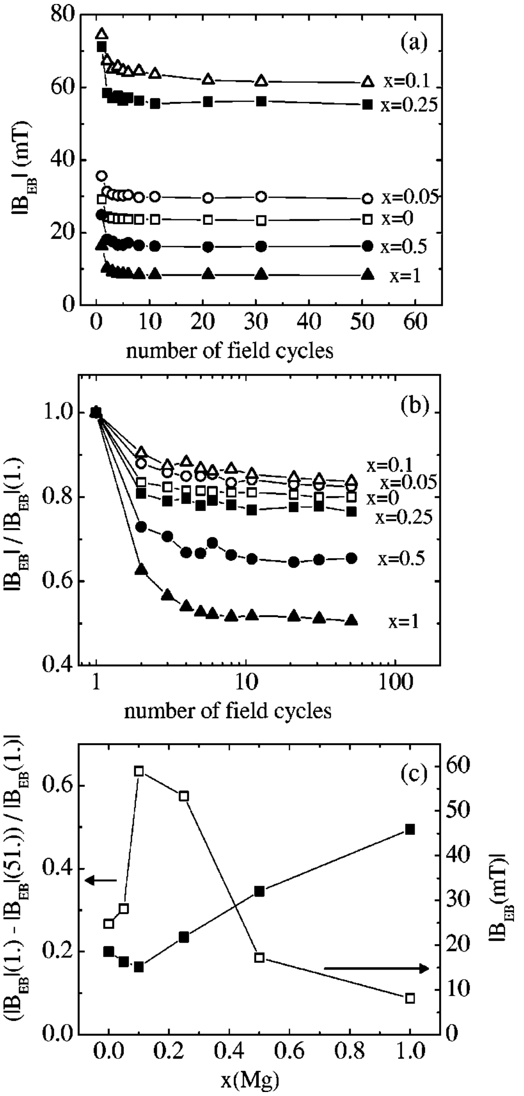

FIG. 10. Dilution dependence of the training effect for Co/Co$_{1-x}$Mg$_x$O samples. (a) EB shift as a function of subsequent hysteresis cycles for different Mg concentrations x at $T=5$ K. (b) Normalized EB values from (a) plotted on a semilog scale. Note that there is almost no training effect after ten field cycles. (c) Relative training effect vs Mg concentration (filled squares) superimposed with absolute EB shift at $T=5$ K from Fig. 6(a).

To further investigate the relevance of the AFM domain structure on the training effect, we focus on its dilution dependence for the Mg-diluted samples (as shown in Fig. 6), which is depicted in Fig.10 at $T=5$ K. Independent of the dilution, the EB shift is strongly reduced only during the first field cycles and then remains almost constant. This behavior is in striking qualitative agreement with MC simulations (see Fig. 9 of Ref. 7).

To further explore the magnitude of the training effect, we plotted the relative decrease of the EB shift by normalizing the data from Fig. 10(a) by their initial value at each dilution. As is seen in Fig. 10(b), the magnitude of this relative training effect behaves nonmonotonically with dilution, with the smallest effect observed for samples near optimum dilution [$x(\mathrm{Mg})=0.1$]. In order to more easily visualize the dilution dependence, we plotted the relative training effect between the first and 51st field cycles as a function of Mg dilutions in Fig. 10(c) as its asymptotic limes together with the absolute EB field values at $T=5$ K. We find that both EB shift and magnitude of the training effect are closely related in their dilution dependence. In other words, at optimum dilution the exchange bias is strongest with the smallest training effect, while at high and low dilution the exchange bias decreases while the training effect is increased.

This supports the notion that the formation of volume domains in the AFM layer plays a crucial role in the exchange bias interaction at the FM/AFM interface. The observed dilution dependence of the training effect can be interpreted within the DS model as follows. Magnetization reversal of the FM layer causes irreversible changes in the AFM domain structure, which yield a reduction of the IDS magnetization m_{IDS} of the AFM interface layer and thus a drop in the EB shift. Energetically, AFM domain walls are most strongly pinned near optimum dilution. This pinning results in large energy barriers and prohibits domain-wall motion upon FM magnetization reversal leading to a small training effect. At larger dilutions the size and the connectivity of the AFM spin lattice gets reduced. This results in a decrease of the AFM domain-wall barrier and a decrease of EB. At the same time AFM domain-wall motion and relaxation become easier upon FM magnetization reversal leading to an enhancement of the training effect.

E. Cooling field dependence

The exchange bias effect reveals a striking dependence on the magnitude of the cooling field B_{FC}. At large cooling fields, the EB is (i) either constant,[37] or moderately reduced in most EB systems, or (ii) changes its sign (positive exchange bias) in systems such as Fe/FeFe$_2$ and Fe/MnFe$_2$.[38,39] These results were explained by antiferromagnetic interface coupling between ferromagnet and antiferromagnet. In the MC simulations, both types of dependencies are qualitatively obtained and can be linked to the sign of the interface coupling.[7] While the former case (i) is obtained for positive (ferromagnetic) FM/AFM interface coupling, a negative (antiferromagnetic) interface coupling yields the latter case (ii).

To investigate the sign of the interface coupling in Co/CoO and its dependence on the AFM volume dilution, we studied the cooling field dependence of the same Co/Co$_{1-y}$O samples as shown in Fig. 6(c) at both low $[p(\mathrm{O}_2)=3.3\times10^{-7}$ mbar$]$ and optimum $[p(\mathrm{O}_2)=5\times10^{-6}$ mbar$]$ defect concentrations. For all cooling fields the FM layer was first magnetized at a field of 5 T and a temperature of $T=320$ K. Then it was cooled to $T=20$ K for cooling fields between $B_{\mathrm{FC}}=0$ T and 5 T. As is shown in Fig. 11, the EB increases at low cooling fields while it slightly decreases at larger fields for both samples. The initial increase we primarily attribute to the magnetization of the FM layer, which is not fully saturated during field cooling at low cooling fields as can be seen in the typical hysteresis loops for the moderately diluted samples at $T=320$ K (see Fig. 4). Since the FM layer magnetization determines the global exchange bias,[40] its decrease towards small fields will reduce the EB coupling.

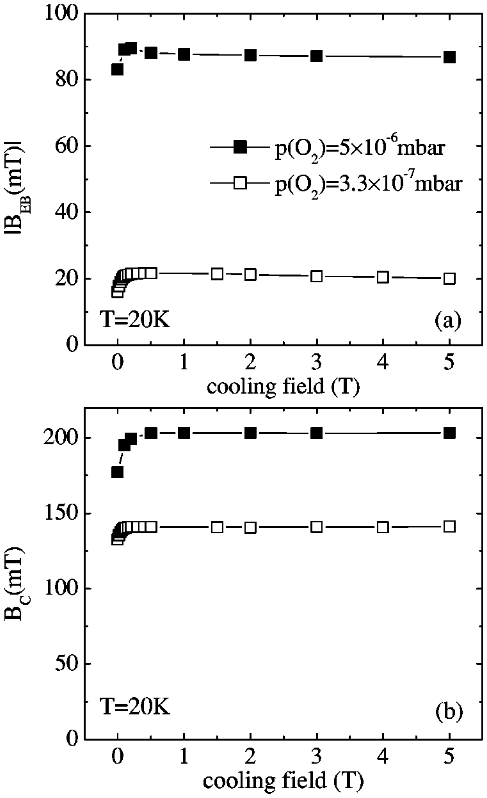

FIG. 11. (a) EB field and (b) coercivity field vs cooling field for Co/Co$_{1-y}$O samples at $T=20$ K with the Co$_{1-y}$O layer prepared at different oxygen pressures.

Because of the only slight decrease of the EB at high cooling fields and no observation of positive EB we conclude that we have positive (ferromagnetic) interface coupling between Co and CoO. This is consistent with no change in sign of B_{EB} in NiFe/CoO up to $B_{\mathrm{FC}}=5$ T.[37] This conclusion is further confirmed by the observation of a positive vertical shift of the hysteresis loops (see Sec. IV A). The Monte Carlo simulations show qualitatively the same EB dependence on the cooling field as observed here for positive interface coupling (see Fig. 10 in Ref. 7). For comparison we plotted the corresponding coercive fields in Fig. 11(b). The same qualitative behavior is observed at low cooling fields as in Fig. 11(a) for B_{EB}, while the coercive field remains constant at larger cooling fields.

F. AFM layer thickness

In the literature there exists no clear statement about the dependence of the exchange bias on the AFM layer thickness. Agreement seems to exist that there has to be a minimum AFM thickness in order to yield EB. For larger thicknesses the observations can be classified into two characteristic types of dependencies.[41,42] (i) For thicknesses larger than a minimum value, the EB remains constant as a function of the AFM layer thickness. (ii) With increasing AFM layer thickness the EB field goes through a maximum

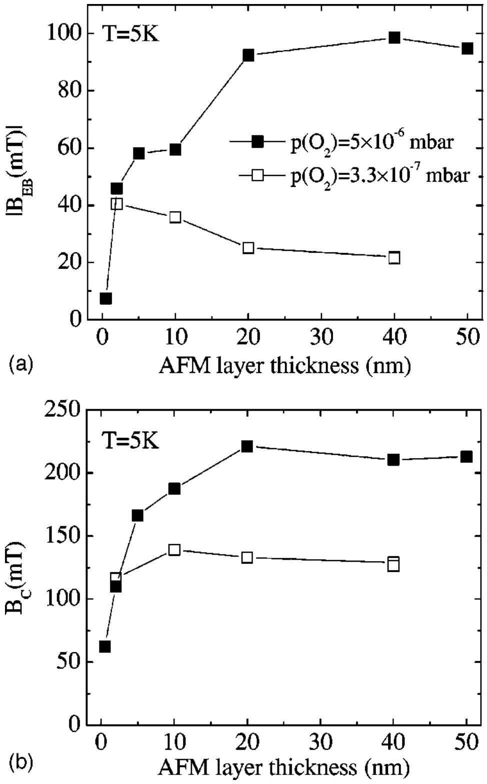

FIG. 12. (a) EB field and (b) coercivity field as a function of the AFM layer thickness in Co/$Co_{1-y}O$ samples for both unintentionally diluted and optimally diluted $Co_{1-y}O$ layers prepared at oxygen pressures of $p(O_2)=3.3\times10^{-7}$ mbar and $p(O_2)=5.0\times10^{-6}$ mbar, respectively.

and then continuously decreases. The AFM layer thickness at which maximum EB occurs or beyond which EB saturates strongly depends on the particular materials chosen as well as on their preparation conditions.

We therefore investigated the AFM layer thickness dependence of the EB field for both unintentionally diluted [$p(O_2)=3.3\times10^{-7}$ mbar] and optimally diluted [$p(O_2)=5\times10^{-6}$ mbar] $Co_{1-y}O$ layers, which is depicted in Fig. 12(a) at $T=5$ K. For optimally diluted samples, the EB field strongly increases with increasing AFM layer thickness and saturates above 20 nm, which roughly corresponds to the size of the AFM crystallites [see Sec. III and Fig. 3(b)]. The EB field for unintentionally diluted samples, however, is decreasing with increasing AFM layer thickness and levels off at large thickness. We note that just by varying the defect density in the volume of the AFM layer we observe both types of thickness dependencies as reported in other EB systems. The MC simulations reproduce this trend (see Fig. 12 in Ref. 7, and Ref. 43) qualitatively.

Within the DS model, these different dependencies are described in the following way. At small levels of disorder (unintentionally diluted samples), AFM domains can only be created at the cost of high energy. Since it is energetically unfavorable to close the domains parallel to the layers, the domain walls will extend through the whole thickness of the AFM layer perpendicular to the FM/AFM interface. For that case, the domain-wall energy increases proportionally to the AFM layer thickness.[11,12] Thus, the formation of a domain wall in the AFM layer becomes less favorable with increasing AFM layer thickness. This results in a reduction of both the number of domain walls and the IDS magnetization m_{IDS}, thus leading to a drop in the EB field with increasing AFM layer thickness. For large AFM layer thicknesses, the low defect density in the volume of the AFM layer prohibits the formation of domain walls even if there is disorder at the interface. For very thin AFM layers, on the other hand, the disorder from the interface dominates and domain-wall formation is energetically favorable, which then leads to a large exchange bias field.

For the optimally diluted samples, domain walls can be created in an external magnetic field at less of a cost of energy due to the nonmagnetic defects. The IDS magnetization m_{IDS} at the interface, which is responsible for the EB, is stabilized by the AFM volume domain structure. This is consistent with the results of the MC simulations.[7] Hence, the domain structure becomes more and more stable with increasing AFM layer thickness leading to an increase of the exchange bias. Assuming that grain boundaries strongly lower the antiferromagnetic coupling strength, the grains may act magnetically independent, leading to a constant exchange bias for AFM thicknesses larger than the grain size. This is consistent with our experimental observations in Fig. 12.

V. CONCLUSIONS

In conclusion, we have tested and demonstrated experimentally that the theoretical DS model for exchange bias,[7] inherently based on disorder in the volume of the AFM layer, gives consistent insight into the mechanism of the exchange bias effect. Most of the characteristic EB phenomena, such as the vertical shift of the hysteresis loop, dilution dependence, temperature dependence, training effect, cooling field dependence, and antiferromagnetic layer thickness dependence, find a consistent description in the combination of structural disorder together with the formation of an antiferromagnetic domain state. The disorder can result from interfacial roughness, defects in the volume part of the AFM, grain boundaries, or from other sources.

The DS model can also account for the large variation of observed EB coupling constants even for identical FM/AFM material systems.[5] Samples of the same FM/AFM material system prepared by different deposition and/or oxidization techniques on various substrates result in a large variation in crystalline, compositional, as well as interfacial properties. Our experimental studies corroborated by MC simulations of the DS model indicate that the AFM domain structure crucially depends on the particular configuration and density of volume defects (such as deficiencies of magnetic atoms or ions) as well as on structural defects (such as grain boundaries, screw dislocations, twin boundaries, and others) in the AFM layer. This results in different spin configurations as well as a different irreversible domain state magnetization m_{IDS} of the AFM interface layer, which cause a strong variation in the exchange bias coupling strength at the FM/AFM interface [see Figs. 6(a) and 6(c)]. As various fabrication techniques and preparation conditions crucially lead to different types of defects and defect concentrations, the AFM domain structure and thus the EB coupling constant appear to be strongly sample dependent. Therefore, for the sake of comparing different EB systems, at least a relative tendency of increasing or decreasing EB field with varying defect concentrations should be known if not a detailed, possibly quantitative analysis of defect concentrations.

Controversies about the dependence of EB on the FM/AFM interface roughness[39,44–50] might also be accounted for by the DS model. Any change of interface roughness due to variations in the preparation parameters, such as growth or annealing temperature, most likely also results in a change of defect structure and domain configuration in the AFM layer, although their mutual interrelation is presently not understood. This model and further more detailed models[51] might eventually explain a variety of additional EB effects not addressed here, such as perpendicular coupling, rotational hysteresis,[52] rotatable anisotropy,[53] asymmetric magnetization reversals,[54,55] and others.

ACKNOWLEDGMENTS

We acknowledge the support of Dr. C. D. Bredel who made high-resolution SQUID magnetometry available to us at the Technical University of Darmstadt. We thank M. Kuhlmann for performing the x-ray measurements as shown in Fig. 3. This work has been supported by the Deutsche Forschungsgemeinschaft through SFB Grant Nos. 341 and 491.

---

*Email address: bernd.beschoten@physik.rwth-aachen.de

†Email address: uli@thp.uni-duisburg.de

[1] W.H. Meiklejohn and C.P. Bean, Phys. Rev. **102**, 1413 (1956).

[2] W.H. Meiklejohn and C.P. Bean, Phys. Rev. **105**, 904 (1957).

[3] R.C.S. Kools, IEEE Trans. Magn. **32**, 3165 (1996).

[4] Satoru Araki, Masashi Sano, Shuxiang Li, Yoshihiro Tsuchiya, Oliver Redon, Tetsuro Sasaki, Noriaki Ito, Kohichi Terunuma, Haruyuki Morita, and Mikio Matsuzaki, J. Appl. Phys. **87**, 5377 (2000).

[5] For a recent review, see J. Nogués and Ivan K. Schuller, J. Magn. Magn. Mater. **192**, 203 (1999).

[6] P. Miltényi, M. Gierlings, J. Keller, B. Beschoten, G. Güntherodt, U. Nowak, and K.D. Usadel, Phys. Rev. Lett. **84**, 4224 (2000).

[7] U. Nowak, K.D. Usadel, J. Keller, P. Miltényi, B. Beschoten, and G. Güntherodt, preceding paper, Phys. Rev. B **66**, 014430 (2002).

[8] W. Kleemann, Int. J. Mod. Phys. B **7**, 2469 (1993).

[9] D. P. Belanger, in *Spin Glasses and Random Fields*, edited by A. P. Young (World Scientific, Singapore, 1998).

[10] A.P. Malozemoff, Phys. Rev. B **35**, 3679 (1987).

[11] A.P. Malozemoff, J. Appl. Phys. **63**, 3874 (1988).

[12] A.P. Malozemoff, Phys. Rev. B **37**, 7673 (1988).

[13] Pieter Kuiper, Barry G. Searle, Petra Rudolf, L.H. Tjeng, and C.T. Chen, Phys. Rev. Lett. **70**, 1549 (1993).

[14] J. Stöhr, A. Scholl, T.J. Regan, S. Anders, J. Lüning, M.R. Scheinfein, H.A. Padmore, and R.L. White, Phys. Rev. Lett. **83**, 1862 (1999).

[15] A. Scholl, J. Stöhr, J. Lüning, J.W. Seo, J. Fompeyrine, H. Siegwart, J.-P. Locquet, F. Nolting, S. Anders, E.E. Fullerton, M.R. Scheinfein, and H.A. Padmore, Science **287**, 1014 (2000).

[16] F.U. Hillebrecht, H. Ohldag, N.B. Weber, C. Bethke, U. Mick, M. Weiss, and J. Bahrdt, Phys. Rev. Lett. **86**, 3419 (2001).

[17] F. Nolting, A. Scholl, J. Stöhr, J.W. Seo, J. Fompeyrine, H. Siegwart, J.-P. Locquet, S. Anders, J. Lüning, E.E. Fullerton, M.F. Toney, M.R. Scheinfein, and H.A. Padmore, Nature (London) **405**, 767 (2000).

[18] H. Ohldag, A. Scholl, F. Nolting, S. Anders, F.U. Hillebrecht, and J. Sthr, Phys. Rev. Lett. **86**, 2878 (2001).

[19] H. Matsuyama, C. Haginoya, and K. Koike, Phys. Rev. Lett. **85**, 646 (2000).

[20] W. Zhu, L. Seve, R. Sears, B. Sinkovic, and S.S.P. Parkin, Phys. Rev. Lett. **86**, 5389 (2001).

[21] C. Kittel, in *Introduction to Solid State Physics* (Wiley, New York, 1971).

[22] M. G. Lagally, D. E. Savage, and M. C. Tringides, in *Reflection High-Energy Electron Diffraction and Reflection Electron Imaging of Surfaces*, edited by P.K. Larsen and P.J. Dobson (Plenum Press, New York, 1987), p. 139.

[23] J. Nogués, C. Leighton, and I.K. Schuller, Phys. Rev. B **61**, 1315 (2000).

[24] Kentaro Takano, R.H. Kodama, A.E. Berkowitz, W. Cao, and G. Thomas, Phys. Rev. Lett. **79**, 1130 (1997).

[25] R. Kannan and Mohindar S. Seehra, Phys. Rev. B **35**, 6847 (1987).

[26] H. Kishi, Y. Kitade, Y. Miyake, A. Tanaka, and K. Kobayashi, IEEE Trans. Magn. **32**, 3380 (1996).

[27] S. Soeya, H. Hoshiya, M. Fuyama, and S. Tadokoro, J. Appl. Phys. **80**, 1006 (1996).

[28] S. Soeya, H. Hoshiya, R. Arai, and M. Fuyama, J. Appl. Phys. **81**, 6488 (1997).

[29] A. Mougin, T. Mewes, M. Jung, D. Engel, A. Ehresmann, H. Schmoranzer, J. Fassbender, and B. Hillebrands, Phys. Rev. B **63**, 060409 (2001).

[30] J. Nogués (private communication).

[31] T.J. Moran, J.M. Gallego, and Ivan K. Schuller, J. Appl. Phys. **78**, 1887 (1995).

[32] J. Nogués, T.J. Moran, D. Lederman, Ivan K. Schuller, and K.V. Rao, Phys. Rev. B **59**, 6984 (1999).

[33] P.J. van der Zaag, Y. Ijiri, J.A. Borchers, L.F. Feiner, R.M. Wolf, J.M. Gaines, R.W. Erwin, and M.A. Verheijen, Phys. Rev. Lett. **84**, 6102 (2000).

[34] D. Stauffer and A. Aharoni, in *Percolation Theory* (Taylor & Francis, London, 1991).

[35] C. Schlenker, S.S.P. Parkin, J.C. Scott, and K. Howard, J. Magn. Magn. Mater. **54-57**, 801 (1986).

[36] S.G.E. te Velthuis, A. Berger, G.P. Felcher, B.K. Hill, and E. Dan Dahlberg, J. Appl. Phys. **87**, 5046 (2000).

[37] T. Ambrose and C.L. Chien, J. Appl. Phys. **83**, 7222 (1998).

[38] J. Nogués, D. Lederman, T.J. Moran, and Ivan K. Schuller, Phys. Rev. Lett. **76**, 4624 (1996)

[39] C. Leighton, J. Nogués, H. Suhl, and Ivan K. Schuller, Phys. Rev. B **60**, 12 837 (1999).

[40] P. Miltényi, M. Gierlings, M. Bamming, U. May, G. Güntherodt, J. Nogués, M. Gruyters, C. Leighton, and Ivan K. Schuller,

Appl. Phys. Lett. **75**, 2304 (1999).
[41] K.T.-Y. Kung, L.K. Louie, and G.L. Gorman, J. Appl. Phys. **69**, 5634 (1991).
[42] O. Allegranza and M.-M. Chen, J. Appl. Phys. **73**, 6218 (1993).
[43] U. Nowak, A. Misra, and K.D. Usadel, J. Appl. Phys. **89**, 7269 (2001).
[44] J. Nogués, T.J. Moran, D. Lederman, Ivan K. Schuller, and K.V. Rao, Phys. Rev. B **59**, 6984 (1999).
[45] J. Nogués, D. Lederman, T.J. Moran, Ivan K. Schuller, and K.V. Rao, Appl. Phys. Lett. **68**, 3186 (1996).
[46] T.J. Moran, J.M. Gallego, and Ivan K. Schuller, J. Appl. Phys. **78**, 1887 (1995).
[47] C.-M. Park, K.-I. Min, and K.H. Shin, IEEE Trans. Magn. **32**, 3422 (1996).
[48] C.-M. Park, K.-I. Min, and K.H. Shin, J. Appl. Phys. **79**, 6228 (1996).
[49] D.-H. Han, J.-G. Zhu, J.H. Judy, and J.M. Sivertsen, J. Appl. Phys. **81**, 340 (1997).
[50] D.G. Hwang, S.S. Lee, and C.M. Park, Appl. Phys. Lett. **72**, 2162 (1998).
[51] U. Nowak, A. Misra, and K.D. Usadel, J. Magn. Magn. Mater. **240**, 243 (2002).
[52] S. Soeya, S. Nakamura, T. Imagawa, and S. Narishige, J. Appl. Phys. **77**, 5838 (1995).
[53] R.D. McMichael, M.D. Stiles, P.J. Chen, and W.F. Egelhoff, Jr., Phys. Rev. B **58**, 8605 (1998).
[54] M.R. Fitzsimmons, P. Yashar, C. Leighton, Ivan K. Schuller, J. Nogués, C.F. Majkrzak, and J.A. Dura, Phys. Rev. Lett. **84**, 3986 (2000).
[55] C. Leighton, M.R. Fitzsimmons, P. Yashar, A. Hoffmann, J. Nogués, J. Dura, C.F. Majkrzak, and Ivan K. Schuller, Phys. Rev. Lett. **86**, 4394 (2001).